Catapulting towards massive and large spatial quantum superposition

Zhou, Run; Marshman, Ryan J.; Bose, Sougato; Mazumdar, Anupam

Published in:
Physical Review Research

DOI:
10.1103/PhysRevResearch.4.043157

Publication date:
2022

Catapulting towards massive and large spatial quantum superposition

Run Zhou,[1] Ryan J. Marshman,[2] Sougato Bose,[3] and Anupam Mazumdar[1]
[1]*Van Swinderen Institute, University of Groningen, 9747 AG Groningen, The Netherlands*
[2]*Centre for Quantum Computation and Communication Technology, School of Mathematics and Physics, University of Queensland, Brisbane, Queensland 4072, Australia*
[3]*Department of Physics and Astronomy, University College London, Gower Street, WC1E 6BT London, United Kingdom*

(Received 23 June 2022; accepted 23 September 2022; published 2 December 2022)

A large spatial quantum superposition of size $O(1–10)$ μm for mass $m \sim 10^{-17}$–10^{-14} kg is required to probe the foundations of quantum mechanics and test the classical and quantum nature of gravity via entanglement in a laboratory. In this paper, we will show that it is possible to accelerate the two spin states of a macroscopic nanocrystal sourced by the inhomogeneous nonlinear magnetic field in a Stern-Gerlach-type setup. We will assume that the electronic spin can be embedded at the center of the nanocrystal, such as the nitrogen-vacancy (NV) center of diamond. Our analysis will be generic to any dopant or any material. We will show that we can create a desired superposition size within 1–2 s by catapulting the trajectories of the two spin states with a modest magnetic field gradient and then recombine the trajectories for a coherent interference. We will show the demanding nature of the precision required in the magnetic field to recover a 99% spin coherence confidence level at the moment of interference.

DOI: 10.1103/PhysRevResearch.4.043157

I. INTRODUCTION

Gravity is one of the weakest interactions of nature, and it is very special because of its universality. Unlike any other known interactions, it is not yet clear whether gravity respects the rules of quantum mechanics at a microscopic level [1]. No experimental proof validates whether the gravitational interaction is indeed quantum. The spacetime we have witnessed so far in gravitational experiments is extremely classical without any hint of quantumness [2].

The conventional wisdom is that the gravitational effects will become important only when we approach the Planckian length or time scale, making it extremely challenging to test the quantum nature of gravity in a laboratory. Furthermore, neither tests from the cosmological perturbations in the cosmic microwave background radiation [3] nor the positive detection of primordial gravitational waves [4] confirms the quantum nature of gravity; as a matter of fact, neither do any other astrophysical tests [5]. They all have many astrophysical uncertainties, making it extremely challenging to conclude the true nature of gravity. Also, the feeble nature of the gravitational interaction makes it extremely hard to detect the graviton as an individual quantum [6].

Despite all these challenges, there is one hope for gravity. The gravitational interaction is a long-range interaction like in the case of quantum electrodynamics, hence it gives us a unique possibility to test its quantum properties in the infrared spectrum.

Recently, a tabletop experiment has been proposed to explore such a quantum origin of gravity with the help of quantum superposition and quantum entanglement [7,8]. The protocol known as the quantum-gravity-induced entanglement of masses (QGEM) is based on the quantum interaction of gravity with the quantum state of matter to generate the entanglement. The latter is purely a quantum observable and has no classical analog. If gravity is indeed quantum, it will entangle the two masses in quantum spatial superpositions [9,10]. In the canonical approach to quantum gravity, the gravitational interaction is being mediated by the hypothetical massless spin-2 graviton, whose quantum properties can be studied [10]; see also Refs. [7,11] for the path integral approach and Ref. [12] for the Arnowitt-Deser-Misner (ADM) approach. The critical point to note here is that a creation of a spatial superposition is governed by its own dynamical degree of freedom, which conserves the equations of motion governed by the electromagnetic properties of the material. To understand the theoretical aspects of the entanglement, we will always need to consider the dynamical aspects of two masses; see Ref. [10].

A large spatial superposition for a massive object tests the foundations of quantum mechanics [13,14], tests the equivalence principle of gravity [15,16], falsifies spontaneous collapse mechanisms [17,18], and places bounds on decoherence mechanisms [19,20]. Furthermore, as an application of a massive quantum interferometer, we can use them as a quantum sensor [21] and to probe very high frequency gravitational waves [22].

To realize some of these ambitious experiments, especially QGEM, we will require a large spatially localized state of

superposition $\Delta Z \sim O(10\text{–}100)\ \mu$m for large masses of order $m \sim 10^{-15}$–10^{-14} kg [7,23]. We are assuming that the superposition is in the z direction. These requirements are far beyond the scales achieved to date in any laboratory (e.g., macromolecules $m \sim 10^{-22}$ kg over $\Delta Z \sim 0.25\ \mu$m, or atoms of mass $m \sim 10^{-25}$ kg over $\Delta Z \sim 0.5$ m [14,24–27]).

Despite numerous challenges, there are already physical schemes to obtain small ΔZ and m [28–52], and there are arguments presented on how to achieve large superposition in a vacuum by using the Stern-Gerlach principle in the presence of a magnetic field gradient [45,50,53]. Based on these ideas, a feasibility experiment has been performed with the help of atoms, showing that such a Stern-Gerlach interferometer (SGI) for massive objects can indeed be realizable [48]. Of course, we will now need to increase the mass by nearly six to seven orders of magnitude, which will pose a serious technical, if not fundamental, challenge.

In this paper, we aim to improve the existing mechanism for creating a large spatial superposition [7,45,50,53]. In this paper we will consider the effect of a spatially dependent nonlinear magnetic field to create the superposition as opposed to the spatially dependent linear magnetic field in Ref. [53]. We will utilize the nonlinear magnetic field profile to further increase the spatial superposition size. We will concentrate on the one-dimensional interferometer, which avoids the issues related to the two-dimensional SGI [54]. We will be focusing on applying a much lower magnetic field gradient *first* described in the original paper about QGEM [7]. We are assuming that the electronic spin can be embedded at the center of the nanocrystal, such as in the case of a nitrogen-vacancy (NV) center in diamond. Our discussions will be generic to any dopant and material, but for illustration, we will use material properties similar to those of diamond. Also, we will avoid the low region of the magnetic field for the Majorana spin flip [55,56], discussed below.

Typically, we will require experimental configurations with a magnetic field which originates in a single current-carrying wire or a permanent magnet, where the magnetic field goes as $|B| \propto 1/z$, where z is the distance from the current source. The magnetic field can then be expanded around a small region. Such configurations were considered in Ref. [53]. However, as we will see below, if we consider the nonlinear part of the magnetic field dependence, we can generate an even larger superposition size at a shorter time scale. Indeed, a detailed discussion of obtaining such a magnetic field profile will require separate consideration, such as a quadrupole field from coils in an anti-Helmholtz configuration.

We will further assume that we can achieve the required level of internal cooling of the nanocrystal and the external cooling for maintaining the coherence of the spin for 1–2 s; see the bounds on ambient temperatures in Refs. [7,23,57]. We will also assume that the crystal is ideal; in this respect, we are assuming that the impurities are very small, such that the spin coherence can be maintained. The internal cooling for the crystal will also suppress the phonon vibration sufficiently to maintain the spin coherence [7]. Given that all these effects are under control, we will ask, how large a superposition size can we achieve for objects of mass 10^{-17}, 10^{-16}, and 10^{-15} kg?

We will apply the inhomogeneous magnetic field profile and the bias magnetic field. We will consider the nonlinear dependence of the magnetic field in one direction, z, without loss of any generality. In this regard, we will create the superposition primarily in the z direction. We will first create a velocity difference between the two paths of the spins by creating anharmonic oscillations and create a sufficiently large velocity difference between the two paths to catapult the trajectories as far as possible to create a large ΔZ. Then we will bring the trajectories back to cause the two paths to interfere, and we will study the spin coherence [58,59].

While creating the spatial superposition, we will lose the spin coherence; therefore, to create interference, we will need to ensure that the spin coherence is restored at the moment of interference. We will demand that the spin coherence be 99%, which will place a severe constraint on the two paths and hence any fluctuations they incur in creating the superposition. We will see that our analysis following Refs. [58,59] will put a stringent constraint on the magnetic field fluctuations, which we can tolerate. We will also assume that the entire setup is performed in a free-fall experiment, such that the Earth's gravitational acceleration can be negligible. The latter is necessary for avoiding any gravity-induced and relative acceleration noise; the details can be found in Ref. [21].

The paper is organized as follows. In Sec. II, we will discuss the foundations of the SGI setup and discusses the nonlinear magnetic field profile and the constraints on the magnetic field. In Sec. III, we will discuss various stages of the two trajectories for masses 10^{-17}, 10^{-16}, and 10^{-15} kg. In Sec. IV, we will discuss the scaling behavior of the superposition size. In Sec. V, we will discuss the constraint on the magnetic field fluctuation, which we can tolerate for the spin coherence, and in Sec. VI, we will conclude our paper.

II. STERN-GERLACH INTERFEROMETER

We can write the Hamiltonian of the spin embedded in the nanocrystal as [45,53,60]

$$H = \frac{\hat{\boldsymbol{p}}^2}{2m} + \hbar D\hat{\boldsymbol{S}}^2 - \frac{\chi_m m}{2\mu_0}\boldsymbol{B}^2 - \hat{\boldsymbol{\mu}}\cdot\boldsymbol{B}, \tag{1}$$

where m is the mass of the nanocrystal and $\hat{\boldsymbol{p}}$ and $\hat{\boldsymbol{S}}$ are momentum and spin operators, respectively. D is the NV zero-field splitting. χ_m is the magnetic susceptibility. μ_0 is the vacuum permeability, $\hat{\boldsymbol{\mu}} = -g\mu_B\hat{\boldsymbol{S}}$ is the spin magnetic moment, where $g \approx 2$ is the Landé g factor, $\mu_B = \frac{e\hbar}{2m_e}$ is the Bohr magneton, e is the electron charge, and m_e is the electron rest mass. $\boldsymbol{B}$ is the magnetic field. We will assume that the spin is embedded in the center of the nanocrystal. We will not consider the effects of external torque in this paper; we are assuming that we can engineer a situation so that the torque and the rotational effects of the mass are negligible or decoupled from the translation (for possible mechanisms to cool rotation, see Refs. [61–65]). At this point, we also consider an idealized system with no impurities. Of course, in reality, we will need to consider the impurities. However, for this toy model, we will not consider these effects here for the time being. Note that we are neglecting the gravitational potential here. We will be interested in experimenting with a free-fall setup to minimize gravity gradient noise and dephasing due to Earth's gravitational potential; see the discussion in Ref. [21].

With these assumptions, the last two terms in Eq. (1) represent the potential energy

$$\hat{U} = -\frac{\chi_m m}{2\mu_0}\boldsymbol{B}^2 - \hat{\boldsymbol{\mu}} \cdot \boldsymbol{B}, \tag{2}$$

from which we can calculate the acceleration of the nanocrystal as

$$\hat{\boldsymbol{a}} = -\frac{1}{m}\nabla\hat{U} = \frac{\chi_m}{2\mu_0}\nabla\boldsymbol{B}^2 - \frac{ge\hbar}{2mm_e}\nabla\hat{\boldsymbol{S}} \cdot \boldsymbol{B}. \tag{3}$$

Equation (3) shows that if the specific form of the magnetic field is determined, then the acceleration can be calculated to obtain the trajectory of the nanocrystal in the magnetic field.

We will assume that the magnetic field takes the following simple form:

$$\boldsymbol{B} = (B_0 + \eta z^2 - \eta x^2)\hat{\boldsymbol{z}} - 2\eta z x\hat{\boldsymbol{x}}, \tag{4}$$

where B_0 is a fixed constant magnetic field. We will explain below why we need this bias magnetic field to align the NV spin in the z direction. The η is a coefficient with the dimension $\mathrm{T/m^2}$, while ηz will determine the magnetic field gradient [66]. Here, we have assumed that at the initial moment the coordinate of the NV center along the x axis is zero ($x = 0$) and that the embedded spin is aligned in the z direction ($S_x = 0$).

Let us now calculate $\nabla\boldsymbol{B}^2 = 2(B_0 + \eta z^2)2\eta z\hat{\boldsymbol{z}}$ and $\nabla\hat{\boldsymbol{S}} \cdot \boldsymbol{B} = (2\eta z S_z)\hat{\boldsymbol{z}}$, respectively, and then combine the results to get the expression for the acceleration.

$$a_z = \left(\frac{\chi_m}{\mu_0}(B_0 + \eta z^2)2\eta z - S_z\frac{ge\hbar}{mm_e}\eta z\right)\hat{\boldsymbol{z}}. \tag{5}$$

The initial state superposition is given by $(|\uparrow\rangle_z + |\downarrow\rangle_z)/\sqrt{2}$, the internal spin of the NV center, and the z direction for the wave packet separation.

The above equation (5) shows that the wave packet only separates in the z direction and that in the x coordinate of the NV center the acceleration is always zero. The spin state in the x and y basis will experience a rapid Larmor precession; therefore averaging the spin yields no net force along the x axis in our case. This means that as long as B_0 in Eq. (4) is not zero, we can ensure that the spin direction is approximately aligned along the z axis and avoid the Majorana spin flips; see Ref. [53]. However, this is an ideal situation. In the actual experiment, the spin would have a Larmor precession around the z axis. The minimum allowable value of B_0 in Eq. (4) can be determined by both the Larmor precession frequency and the adiabatic condition of the frequency which forbids the particle motion along the x axis; see, for details, Ref. [53]. The Larmor precession frequency is given by

$$\omega_L = \frac{ge}{2m_e}|\boldsymbol{B}(\boldsymbol{x}, \boldsymbol{z})|, \tag{6}$$

which will be required to satisfy the adiabatic condition $\dot{\omega}_L \ll \omega_L^2$ [53]. Combining Eqs. (4) and (6), and the adiabaticity condition, we are able to obtain the minimum magnetic field, labeled $B_{\min}$. The minimum Larmor precession frequency corresponding to the minimum magnetic field that satisfies the adiabatic condition is

$$\omega_L^{\min} = \frac{ge}{2m_e}B_{\min}. \tag{7}$$

In this paper, we will set $B_0 \geqslant B_{\min}$, and B_0 is the minimum magnetic field coordinates experienced by the wave packet; so the adiabatic condition is always satisfied during the evolution of the wave packet. We will take $B_0 \approx 5.7 \times 10^{-4}$ T, which ensures that the adiabatic condition is always satisfied in this paper.

III. CATAPULTING TRAJECTORIES

Note that the difference between the two wave packet trajectories is mainly caused by the difference in the spin eigenvalues of the second term on the right-hand side in Eq. (5). We would expect to get a large superposition size by increasing the value of η. However, increasing the value of η will only increase the motional frequency of the wave packet and will not directly increase the superposition size ΔZ. Furthermore, it maintains the superposition size for a longer period. We clearly see this result in Fig. 1. When we fix the mass of the nanocrystal and increase the value of η, we find that the motional frequency of the wave packet increases with η while the maximum superposition size remains almost unchanged, such that it can reach $\Delta Z \sim 40$ μm within $\tau \sim 1.2$ s for the case $m = 10^{-17}$ kg. Similar results were found for the other two masses considered.

Although the superposition size does not increase with η, we can increase the velocity difference between the two wave packets in a short time by increasing the value of η (as shown in Fig. 2). When there is a large velocity difference between the two wave packets and the spatial position coincides, we can adjust the magnetic field so that the two wave packets are located at the lowest point of the potential energy (which is $z = 0$). By doing so, we can catapult the two wave packets around in the magnetic field and achieve a large superposition size.

We will now discuss the trajectories of the wave packets. Let us first consider the case where the nanocrystal has a mass of 10^{-17} kg. A similar analysis will arise for all the other masses under consideration. We will discuss the implementation in three stages. The purpose of the first stage is to obtain a large velocity difference between the two trajectories in a short time (around, say, 0.2 s) by applying ($\eta = 1 \times 10^8$ $\mathrm{T/m^2}$) [67]. The purpose of the second stage is to generate, and then close, a large spatial superposition of the two trajectories. To do this, we decrease the acceleration of the wave packets by decreasing the value of η. By adjusting the value of η to an appropriate value, we can get a large superposition size in a relatively short coherent time scale ($\sim$1 s) [69,70]. When the spatial positions of the two wave packets coincide again, we begin the third stage. We then adjust the magnetic field gradient and the position of the particle in the potential energy. Doing so carefully will close the interferometer, causing the spatial and momentum differences to become zero in both arms (Fig. 3). Figure 4 shows these steps graphically. The behavior of the nanocrystals in the magnetic field for masses of 10^{-16} and 10^{-15} kg is very similar to that for a mass of 10^{-17} kg, and we have included the numerical results for both those cases (10^{-16} and 10^{-15} kg) in Appendix C. We can also consider these stages in more detail.

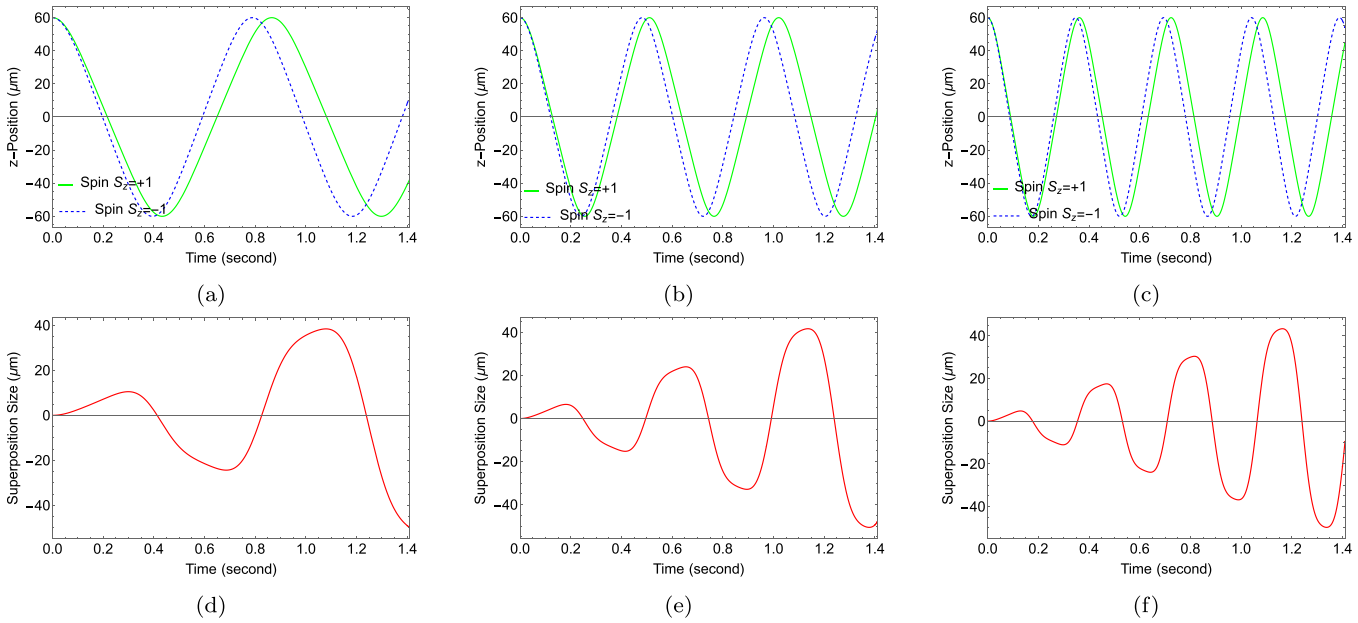

FIG. 1. Trajectories of the two wave packets under different magnetic field gradients and the corresponding superposition size. η is a parameter associated with the magnetic field profile. With the increase in the value of η [(a) and (d) 1.4×10^6, (b) and (e) 2.4×10^6, and (c) and (f) 3.4×10^6 T/m^2], the motional frequency of the wave packet increases accordingly, but the maximum superposition size that can be achieved over the same period of time remains almost unchanged (the maximum superposition size is about 40 μm within 1.2 s). The mass here is 10^{-17} kg.

Initialization, $t = 0$. The wave packet enters the inhomogeneous magnetic field region. The initial velocity along the z direction is $\dot{z}(0) = 0$, and the initial position $z_0 = 0$. The parameter $\eta = 1 \times 10^8$ T/m^2.

Stage I, $0 < t < T_1$. The two wave packets oscillate rapidly in the magnetic field, and the velocity difference between them grows larger and larger; see Figs. 4(a) and 4(g). The magnetic field gradient is $\eta z \approx -1 \times 10^4$ T/m at $t = T_1$, where $\eta = 1 \times 10^8$ T/m^2, $z \approx -1 \times 10^{-4}$ m.

At $t = T_1$. Since the difference in the change in the spatial position [Fig. 4(j)] between the two wave packets is opposite to that of the difference in the velocity, it is possible to find a moment when the velocity difference is large enough and the superposition size is 0. This moment is marked T_1. At time

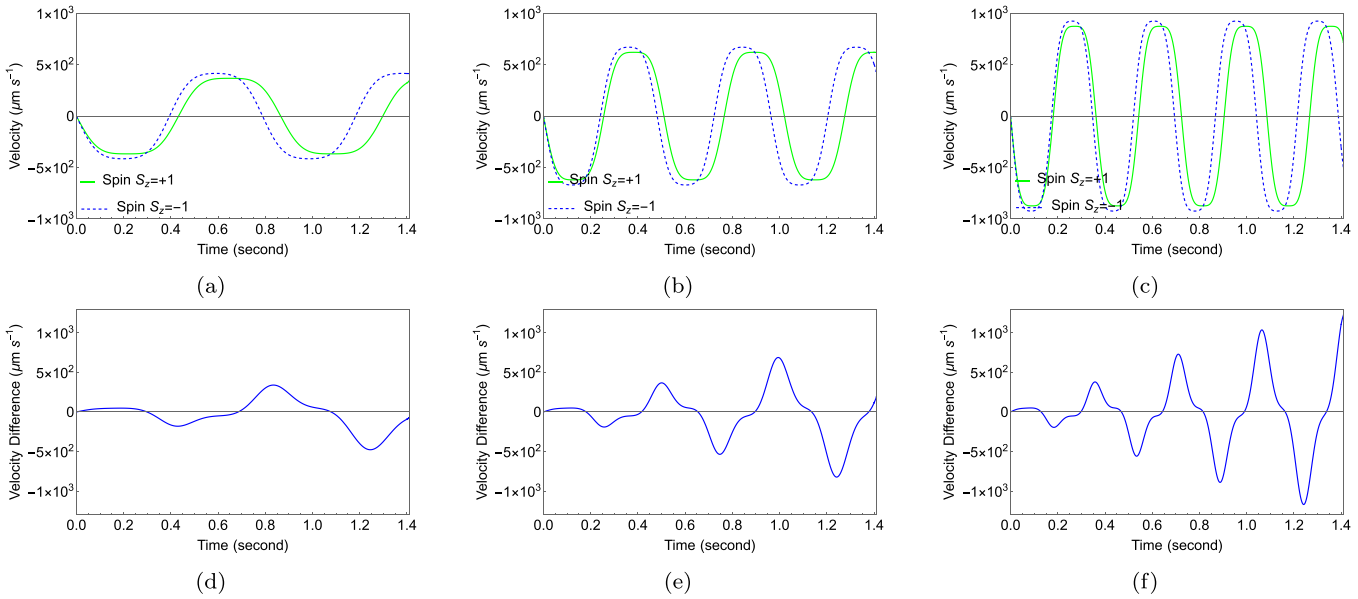

FIG. 2. The velocity curve for the two wave packets under different η and the corresponding velocity difference. By increasing the value of η [(a) and (d) 1.4×10^6, (b) and (e) 2.4×10^6, and (c) and (f) 3.4×10^6 T/m^2], the maximum velocity difference that can be achieved over the same period of time also increases (around 400, 700, and 1100 μm/s in less than 1.2 s, respectively). The mass here is 10^{-17} kg.

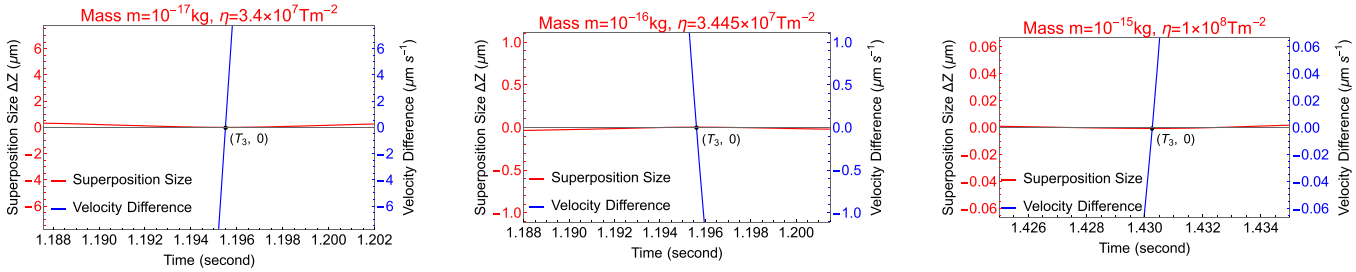

FIG. 3. The velocity difference and the superposition size when the two wave packets' trajectories are closed for the interference for (a) $m = 10^{-17}$ kg, (b) $m = 10^{-16}$ kg, and (c) $m = 10^{-15}$ kg. Here, T_3 has different values for the different masses.

T_1, if we adjust the magnetic field such that the coordinate of the two wave packets in the magnetic field is $z = 0$ [see Fig. 4(b)], then we find the value of $\eta \sim 1 \times 10^5$ T/m^2, and $\partial B_z = \eta z = 0$ at $z = 0$.

Stage II , $T_1 < t < T_2$. In this stage, the two wave packets have different initial velocities at the new initial potential position, which is equivalent to ejecting the two wave packets away from each other. Moreover, due to the reduction in the magnetic field gradient, the spatial position difference between the two wave packets can be significantly increased; see Fig. 4(k).

At $t = T_2$. The two wave packets meet again after a half time period of motion, and we mark the time of their meeting as T_2; see Fig. 4(b). At time T_2, we need to adjust the coordinates of the wave packet in the magnetic field and select an appropriate value of η, so that the trajectory of the two wave packets can be closed in a relatively short time (∼1 s). At time T_2, the magnetic field of the wave packet is adjusted to $z_{T_2} = -102.8$ μm. Parameter η is adjusted to 3.4×10^7 T/m^2.

Stage III , $T_2 < t < T_3$. The two wave packets still oscillate rapidly in the magnetic field, but their spatial position difference and velocity difference will be smaller and smaller; see Figs. 4(i) and 4(l).

At $t = T_3$. The trajectories of the two wave packets are closed. The superposition size is zero, and the velocity difference is zero; see Fig. 3(a). We will analyze this case separately in the context of spin coherence.

In this experimental setup, the magnetic field was changed twice, but we did not consider the effect of the change in the magnetic field here. Note that the magnetic field changes in a short time, so it will only cause a small disturbance to the wave packet trajectory, but we are here taking this effect to be negligible. In fact, we can introduce switching functions of the magnetic field, for example, as discussed in Ref. [53], and our main results will not be adversely affected. It is worth noting that the parameter η used in stage I is as high as 10^8 T/m^2, and the corresponding maximum magnetic field gradient is $\partial B_z \sim 10^4$ T/m (which can be achieved in the laboratory [71]), since the maximum magnetic field coordinates experienced by the wave packet is only 100 μm [see Fig. 4(a) and Appendix C, Figs. 15(a) and 16(a), for different masses].

Since we initialize the coordinates of the NV center in the magnetic field in stage II and stage III , the coordinates of the NV center in the magnetic field are inconsistent with their spatial coordinates in the latter two stages. To avoid confusion, unless otherwise specified, the coordinates mentioned in this paper refer to the coordinates of the NV center in the magnetic field.

We have set the value of η at the first stage to be $\eta \sim 1 \times 10^8$ T/m^2, which limits the time of the first stage to about 0.2 s, and we set the limit of the time of the second stage to about 0.5 s and require the trajectories of the two wave packets to be closed within 1.5 s; then we can get the motion of the wave packets and the superposition size with different masses as shown in Fig. 4 and Appendix C, Figs. 15 and 16.

IV. SCALING BEHAVIOR

We can use Eq. (5) to roughly analyze the motion of the wave packet for any masses. By substituting the values of each physical quantity into Eq. (5), it can be shown that when the mass $m \geqslant 10^{-17}$ kg, the motion of the wave packet is mainly dominated by ηz^2 in the first term on the right-hand side of the equation. This term has nothing to do with mass; that is, as long as the values of η and the initial position are determined, the maximum velocity of the wave packet can be determined. This result can be seen in Fig. 4(d) and Appendix C, Figs. 15(b) and 16(b). The velocity difference between the two wave packets is caused by the second term on the right-hand side of Eq. (5). The value of this term is inversely proportional to the mass. Since the size of the velocity difference determines the superposition size, the maximum superposition size we can achieve should also be inversely proportional to the mass, i.e., $\Delta Z \sim 1/m$. This result is also borne out from our numerical results, as shown in Fig. 4(k) and Appendix C, Figs. 15(k) and 16(k).

It should be noted that in order to compare the behavior of the wave packets with different masses, the values of η and the initial position are chosen properly at different stages of the experiment, but this does not mean that for the wave packets with different masses we can only take these parameter values. For example, if we do not limit the time of the second stage of the experiment to about 0.5 s, we can choose a smaller value of η and get a larger superposition size.

We first perform a linear fitting of the velocity difference in stage I . The fitting formula is

$$\Delta V_{\text{fit}} = \left(\frac{5.4 \times 10^{-13}\ \text{kg}}{m}\right)\left(\frac{T_1}{1\ \text{s}}\right)10^{-6}\ \text{m/s}, \qquad (8)$$

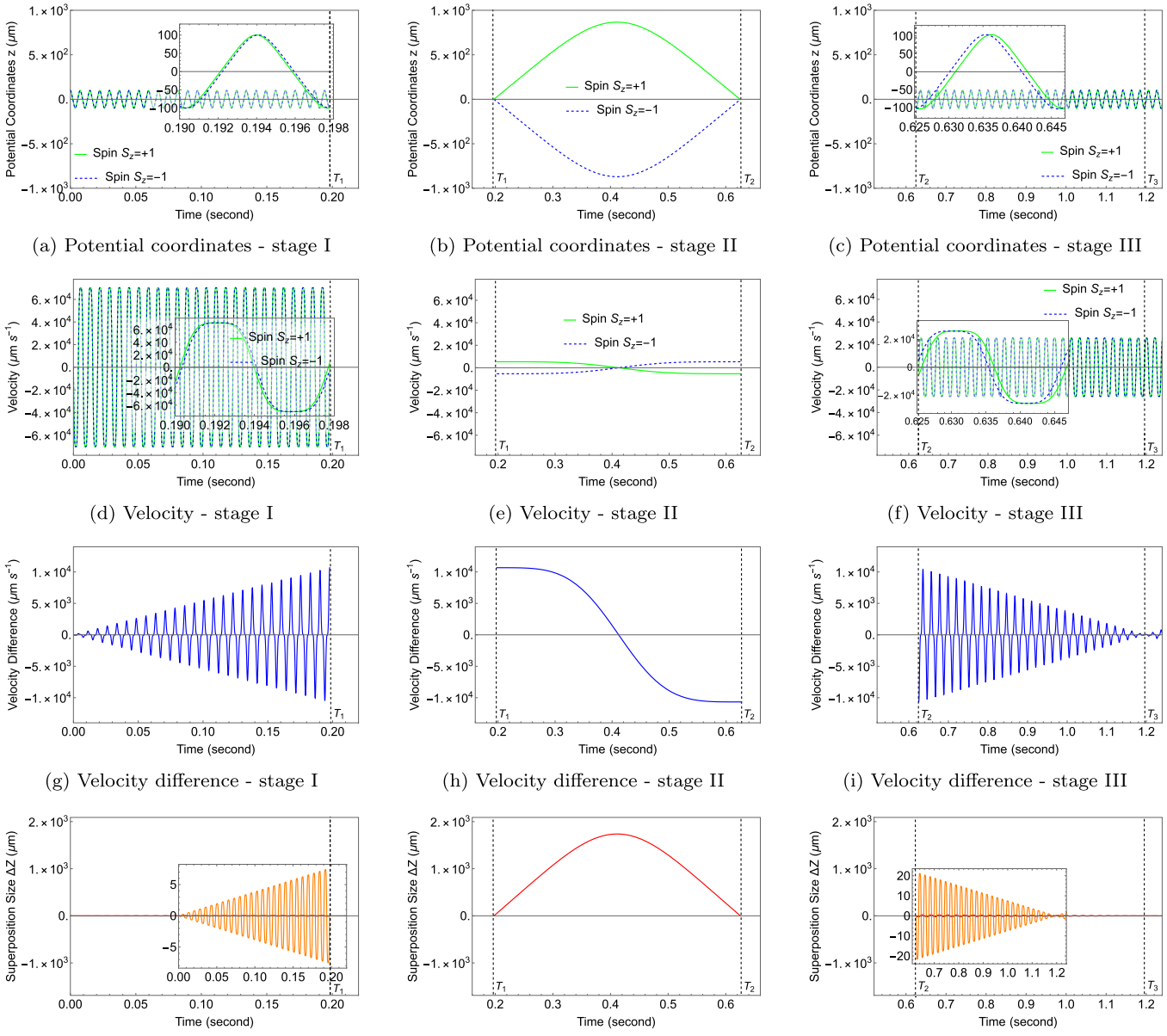

(a) Potential coordinates - stage I (b) Potential coordinates - stage II (c) Potential coordinates - stage III

(d) Velocity - stage I (e) Velocity - stage II (f) Velocity - stage III

(g) Velocity difference - stage I (h) Velocity difference - stage II (i) Velocity difference - stage III

(j) Superposition size - stage I (k) Superposition size - stage II (l) Superposition size - stage III

FIG. 4. Dynamical aspects for the mass $m = 10^{-17}$ kg during the three experimental stages: (a)–(c) the magnetic field coordinates (potential coordinates) experienced, (d)–(f) the velocities, (g)–(i) the velocity differences, and (j)–(l) the superposition size. We set different values of η and the initial position of the wave packet in the magnetic field at different stages. Stage I, $\eta = 1 \times 10^8$ T/m^2, with an initial coordinate $z = 100$ μm. Stage II, $\eta = 1 \times 10^5$ T/m^2, with an initial coordinate $z = 0$ μm. Stage III, $\eta = 3.4 \times 10^7$ T/m^2, with an initial coordinate $z = -102.8$ μm. The initial coordinates here refer to the initialization coordinates of the NV center in the magnetic field at different experimental stages. Times T_1 and T_2 are determined by constraining the moment when the superposition size is zero (with an accuracy of 10^{-6} μm). Time T_3 is the moment when both the velocity difference between the two wave packets and the superposition size are zero.

where ΔV_{fit} is the maximum velocity difference reached in stage I. T_1 is a variable here, representing the end time of stage I. The values of mass m are 10^{-17}, 10^{-16}, and 10^{-15} kg, respectively. The linear fitting results are shown in Fig. 5.

Next, we take the velocity difference obtained in stage I as the initial velocity of the wave packet to study the trajectory of the wave packet in stage II. In Sec. V and Appendix A we discuss the fitting of wave packet trajectories. Now we only need to move the simple harmonic motion [Eq. (26)] by the $-\pi/2$ phase to fit the trajectory of the wave packet with the initial velocity V_{fit} and initial position $z = 0$. The fitting formula of the wave packet trajectory in stage II is

$$z(t) = \Delta Z_0 \cos\left(\sqrt{A}t - \frac{\pi}{2}\right), \tag{9}$$

where ΔZ_0 and $\sqrt{A}$ are the amplitude and frequency of the wave packet motion, respectively. The specific expression of A is found later, in Eq. (27). Combining Eqs. (8) and (9) gives

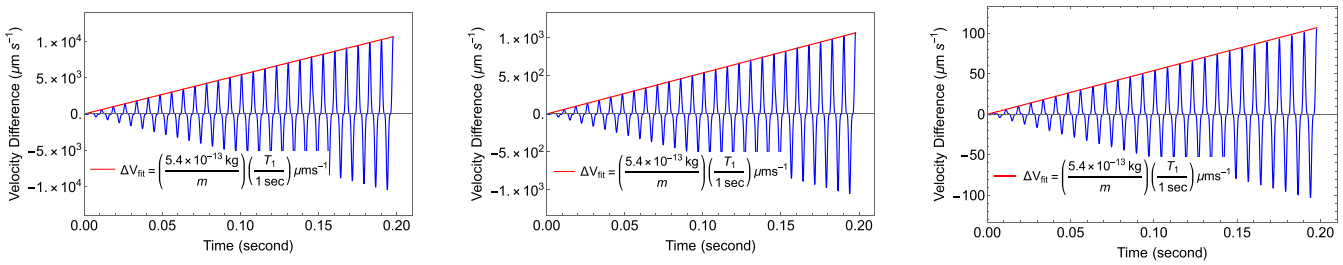

FIG. 5. The linear fitting of the velocity difference for stage I under different masses. The red solid line is a linear fitting of the maximum velocity difference. T_1 is a variable here, representing the end time of stage I. The masses from left to right are 10^{-17}, 10^{-16}, and 10^{-15} kg, respectively. We have set $\eta = 1 \times 10^8$ T/m^2.

the amplitude, and thus maximum superposition size, as

$$\Delta Z_0 = \frac{\Delta V_{\rm fit}}{\sqrt{A}} = \left(\frac{5.4 \times 10^{-13}\ {\rm kg}}{m}\right)\left(\frac{1\ {\rm Hz}}{\sqrt{A}}\right)\left(\frac{T_1}{1\ {\rm s}}\right)10^{-6}\ {\rm m}. \tag{10}$$

For the sake of discussion, let $\sqrt{A} = (\pi/0.4)$ Hz. That is, the half period of wave packet motion is 0.4 s, which is consistent with the time set in stage II of the experiment in this paper. It can be seen from Eq. (10) that the maximum superposition size of the ejection trajectory is inversely proportional to the mass of the nanocrystal. The scaling behavior of the superimposed size is shown in Fig. 6.

This formula is similar to Eq. (11) of Ref. [53]. In Ref. [53], we only considered the magnetic field gradient, so there is only one parameter in the equation. In our case, we need to consider the initial velocity of the wave packet in addition to the gradient, so we need to add a parameter T_1, which represents the initial velocity of the wave packet. If we fix the value of T_1, that is, the magnitude of the initial velocity, then our expression is the same as Eq. (11) of Ref. [53]. However, since we have two parameters to play with, we obtain a larger size of superposition compared with Ref. [53]. For instance, for $m = 10^{-15}$ kg, we can obtain $\Delta Z = 16$ μm with our current proposal in a total time of flight of roughly 1.4 s. In Ref. [53], we had obtained $\Delta Z = 0.11$ μm for the same time period.

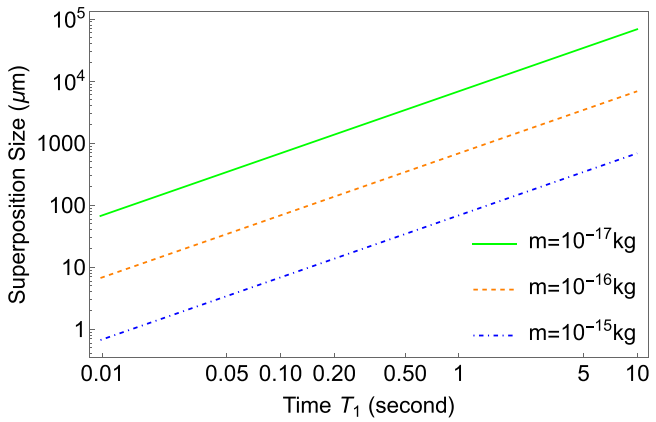

FIG. 6. The scaling behavior of the superposed size (stage II) under different masses obtained by catapulting the trajectories. The maximum superposition size we can achieve is inversely proportional to the mass of the nanocrystal. Here, $\sqrt{A} = \pi/0.4$ Hz.

When discussing the scaling behavior of the superposition size by numerically fitting the velocity difference in stage I and the trajectory of the wave packet in stage II, we should make the following points.

(i) The maximum velocity difference achieved in stage I is determined by the gradient parameter η and the initial position of the nanocrystal in stage I. The greater the value of η and the initial position, the greater the maximum velocity difference. The fitting formula for the velocity difference in Eq. (8) only holds for $\eta = 1 \times 10^8$ T/m^2, initial position $= 100$ μm.

(ii) Time T_1 in Eq. (8) is a variable, with an upper bound determined by both the maximum velocity difference and the mass of the nanocrystal. In this paper, the maximum velocity difference that can be achieved in stage I is about 1.4×10^5 μm/s. Therefore the upper bound on T_1 is about 2.6, 26, and 260 s for masses equal to 10^{-17}, 10^{-16}, and 10^{-15} kg, respectively.

(iii) As can be seen from Eq. (10), by decreasing the value of $\sqrt{A}$, we can get a larger superposition size, but correspondingly, we also need a longer time to close the wave packet trajectory.

(iv) In Eq. (8), the reason for using the velocity difference obtained in stage I to calculate the amplitude directly is that the velocity of the two wave packets corresponding to the linear fitting velocity difference in stage I is almost the same with the direction being opposite. The amplitude calculated from the velocity difference is equal to the sum of the amplitudes of the two wave packets and gives the maximum superposition size.

V. RECOVERING SPIN COHERENCE

The SGI splits the two wave packets in the superposition state. First, they lose their spin coherence and then recombine to recover the spin coherence. We first use the definition of the spin coherence given in Ref. [59] to calculate the expression of the spin coherence in the case of our magnetic field profile and then study what experimental conditions are needed to recover the spin coherence. Heisenberg's equation of motion is given by

$$i\hbar\frac{d\hat{A}_H(t)}{dt} = [\hat{A}_H(t), \hat{H}_H(t)], \tag{11}$$

where $\hat{A}_H(t)$ and $\hat{H}_H(t)$ are the Hermitian and the Hamiltonian operator in the Heisenberg picture, respectively. Using

Eq. (11), we can get the equation of motion for the position,

$$\frac{d\hat{\boldsymbol{r}}(t)}{dt} = \frac{1}{i\hbar}[\hat{\boldsymbol{r}}(t), \hat{H}_H(t)] = \frac{\boldsymbol{p}(t)}{m}, \tag{12}$$

and the equation of motion for the momentum,

$$\begin{aligned}\frac{d\hat{\boldsymbol{p}}(t)}{dt} &= \frac{1}{i\hbar}[\hat{\boldsymbol{p}}(t), \hat{H}_H(t)] \\ &= \frac{\chi_m m}{2\mu_0}\nabla(\boldsymbol{B}[\boldsymbol{r}(t)]^2) + \nabla(\boldsymbol{\mu}(t)\cdot\boldsymbol{B}[\boldsymbol{r}(t)]).\end{aligned} \tag{13}$$

By integrating Eqs. (12) and (13), the formal solution of the evolution of the position and the momentum with time can be written as [59]

$$\begin{aligned}\boldsymbol{p}(t) = \boldsymbol{p}_0 + \int_0^t \Big(&\frac{\chi_m m}{2\mu_0}\nabla(\boldsymbol{B}[\boldsymbol{r}(t')]^2) \\ &-\nabla(\mu_B\boldsymbol{\sigma}\cdot\boldsymbol{B}[\boldsymbol{r}(t')]a^\dagger(t')a(t'))\Big)dt',\end{aligned} \tag{14}$$

$$\begin{aligned}\boldsymbol{r}(t) = \boldsymbol{r}_0 + \frac{t}{m}\boldsymbol{p}_0 + \frac{1}{m}\int_0^t (t-t')\Big(&\frac{\chi_m m}{2\mu_0}\nabla(\boldsymbol{B}[\boldsymbol{r}(t')]^2) \\ &-\nabla(\mu_B\boldsymbol{\sigma}\cdot\boldsymbol{B}[\boldsymbol{r}(t')]a^\dagger(t')a(t'))\Big)dt',\end{aligned} \tag{15}$$

where $\boldsymbol{r}_0$ and $\boldsymbol{p}_0$ are the initial position and the momentum, respectively, $\boldsymbol{\sigma}$ is the spin operator, and $a^\dagger(t)$ and $a(t)$ are creation and annihilation operators with $\boldsymbol{S}(t) = \boldsymbol{\sigma}a^\dagger(t)a(t)$. Since the beams' trajectories are split by an inhomogeneous magnetic field along the z direction, the wave packet motion along the z direction is studied next. With a bit of rearrangement, Eqs. (14) and (15) become

$$p_z(t) - p_z = \Delta p_z, \tag{16}$$

$$z(t) - z_0 - \frac{t}{m}p_z = \Delta z, \tag{17}$$

where

$$\Delta p_z = \int_0^t \Big(\frac{\chi_m m}{2\mu_0}\frac{\partial}{\partial z}B_z(t')^2 - \mu_B\sigma_z\frac{\partial}{\partial z}B_z(t')\Big)dt', \tag{18}$$

$$\Delta z = \frac{1}{m}\int_0^t (t-t')\Big(\frac{\chi_m m}{2\mu_0}\frac{\partial}{\partial z}B_z(t')^2 - \mu_B\sigma_z\frac{\partial}{\partial z}B_z(t')\Big)dt' \tag{19}$$

are the variations in the z component of the position and the momentum. r_z and p_z are the initial z component of the position and the momentum, respectively. We take into account that the wave function of a massive particle localized in the position space at $t = 0$ is a Gaussian wave packet

$$\psi(z,0) = \left(\frac{1}{2\pi\delta z^2}\right)^{1/4} e^{-\frac{z^2}{4\delta z^2}}, \tag{20}$$

with a minimum uncertainty $\delta z\delta p_z = \hbar/2$. In Appendix B, we study the evolution of the wave packet in the presence of the nonlinear magnetic field. We show that the expected value of the position of each arm of the interferometer coincides with the classical trajectories in Eq. (5).

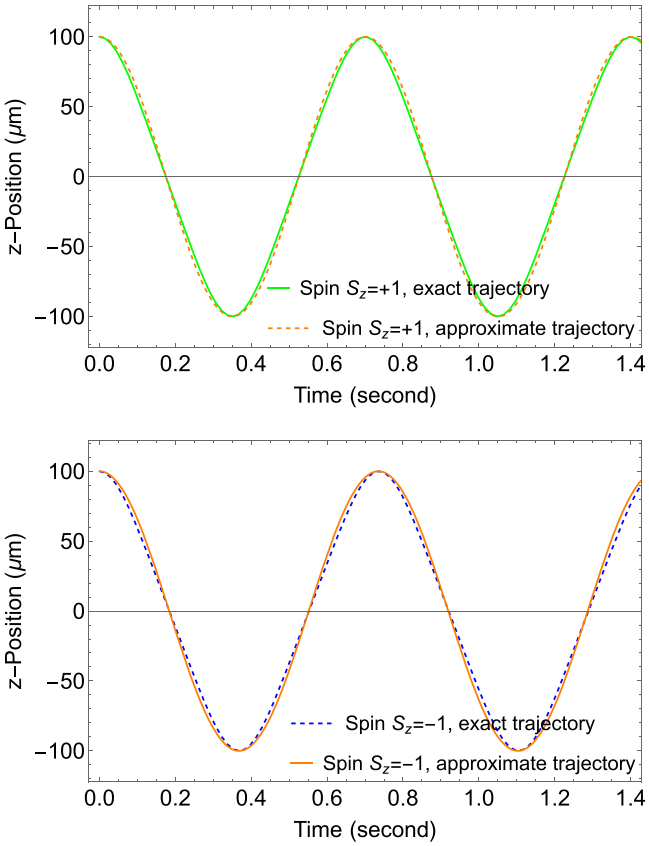

FIG. 7. Comparison of the approximate and exact trajectories of the two wave packets. Here, $m = 10^{-17}$ kg, $\eta = 1 \times 10^6$ T/m^2, and $C_{\text{correct}} = 27.3467$.

In this situation, the spin coherence can be written as [58,59]

$$\langle\hat{\sigma}_x(t)\rangle = \cos[\Phi(t)]\exp\left(-\frac{1}{2}\left[\left(\frac{\Delta z}{\delta z}\right)^2 + \left(\frac{\Delta p}{\delta p}\right)^2\right]\right), \tag{21}$$

where

$$\Phi(t) = \frac{1}{\hbar}g\mu_B\int_0^t B_z(t')dt' \tag{22}$$

is the accumulated Larmor precession angle. We are evaluating the expectation value with respect to the spin state $\frac{1}{\sqrt{2}}(|\uparrow\rangle_z + |\downarrow\rangle_z)$. If $\Phi(t) = 2n\pi$ (n is an integer), $\Delta z = 0$, and $\Delta p = 0$, then $\langle\hat{\sigma}_x(t)\rangle = 1$, and the spin coherence is completely restored. In real experiments, we cannot control the experimental conditions with arbitrary precision. Assume that the experimental error is bounded by certain parameters, given by [58]

$$|\delta\Phi(t)| \leqslant \varepsilon_1, \quad \left|\frac{\Delta z(t)}{\delta z}\right| \leqslant \frac{\varepsilon_2}{\sqrt{2}}, \quad \left|\frac{\Delta p(t)}{\delta p}\right| \leqslant \frac{\varepsilon_3}{\sqrt{2}}, \tag{23}$$

where ε_1, ε_2, and ε_3 are much less than 1, and the specific value depends on our requirements of the experimental accuracy. Performing Taylor expansion of Eq. (21) and then taking

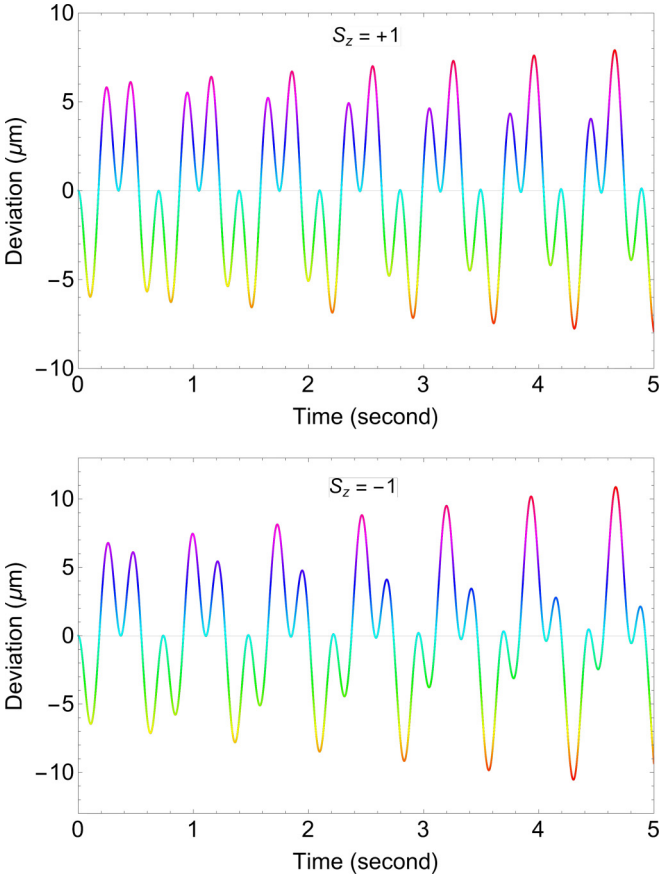

FIG. 8. The deviation between the approximate trajectory and the exact trajectory. Here, $m = 10^{-17}$ kg, $\eta = 1 \times 10^6$ T/m^2, and $C_{\text{correct}} = 27.3467$.

the first-order term gives

$$\langle \hat{\sigma}_x(t) \rangle \lesssim 1 - \frac{1}{2}\left(|\delta\Phi(t)|^2 + \left|\frac{\Delta z(t)}{\delta z}\right|^2 + \left|\frac{\Delta p(t)}{\delta p}\right|^2 \right) \leqslant 1 - \varepsilon^2. \tag{24}$$

Here, we assumed $\varepsilon_1 = \varepsilon_2 = \varepsilon_3 = \varepsilon$ for simplicity. When $\varepsilon = 0.1$, the confidence level for spin coherence is 99%. Next,

TABLE I. Constraints on the magnetic field accuracy required for different masses. The value of spin S_z does not affect the order of the magnitude of accuracy required in η. We have demanded that we recover the spin coherence up to 99%. This table shows the constraints on the magnetic field accuracy from stage II of the trajectory. Similar constraints on η for the stage I part of the trajectory can be found; see Appendix A, Table II.

Mass (kg)	S_z	$(\frac{\Delta\eta}{\eta})_z$	$(\frac{\Delta\eta}{\eta})_{p_z}$
10^{-17}	1	$\lesssim 3.7 \times 10^{-4}$	$\lesssim 6.9 \times 10^{-8}$
	-1	$\lesssim 3.8 \times 10^{-4}$	$\lesssim 7.1 \times 10^{-8}$
10^{-16}	1	$\lesssim 2.1 \times 10^{-4}$	$\lesssim 2.2 \times 10^{-8}$
	-1	$\lesssim 2.1 \times 10^{-4}$	$\lesssim 2.2 \times 10^{-8}$
10^{-15}	1	$\lesssim 1.2 \times 10^{-4}$	$\lesssim 6.9 \times 10^{-9}$
	-1	$\lesssim 1.2 \times 10^{-4}$	$\lesssim 7.0 \times 10^{-9}$

TABLE II. Constraints on the magnetic field accuracy for different masses during stage I. The bounds on η are based on recovering 99% spin coherence. The value of spin S_z does not affect the order of magnitude of the accuracy.

Mass (kg)	S_z	$(\frac{\Delta\eta}{\eta})_z$	$(\frac{\Delta\eta}{\eta})_{p_z}$
10^{-17}	1	$\lesssim 9.3 \times 10^{-6}$	$\lesssim 4.3 \times 10^{-11}$
	-1	$\lesssim 9.3 \times 10^{-6}$	$\lesssim 4.3 \times 10^{-11}$
10^{-16}	1	$\lesssim 5.2 \times 10^{-6}$	$\lesssim 1.4 \times 10^{-11}$
	-1	$\lesssim 5.2 \times 10^{-6}$	$\lesssim 1.4 \times 10^{-11}$
10^{-15}	1	$\lesssim 2.9 \times 10^{-6}$	$\lesssim 4.3 \times 10^{-12}$
	-1	$\lesssim 2.9 \times 10^{-6}$	$\lesssim 4.3 \times 10^{-12}$

we need to make an approximation for Eq. (5), so that we can analytically solve the equation of motion, which is convenient for estimating the trajectory deviation caused by the imprecision of magnetic field control.

We model Eq. (5) with the following acceleration expression:

$$\frac{d^2z(t)}{dt^2} = a_z = \left(C_{\text{correct}} \frac{\chi_m}{\mu_0} B_0 - S_z \frac{ge\hbar}{mm_e} \right) \eta z, \tag{25}$$

where C_{correct} is a dimensionless correction factor. The value of this correction factor is related to η. When η is taking different values, we need to adjust the correction factor to make the approximate trajectory as close to the exact trajectory as possible.

In this paper, we have considered the masses $m \sim 10^{-17}$, 10^{-16}, and 10^{-15} kg; substituting the values of other physical quantities into Eq. (25), we can find that the coefficient $(C_{\text{correct}} \frac{\chi_m}{\mu_0} B_0 - S_z \frac{ge\hbar}{mm_e}) < 0$, which gives rise to the following harmonic oscillator equation with a solution of Eq. (25):

$$z(t) = z_0 \cos(\sqrt{A}t), \tag{26}$$

where A is the square of frequency

$$A = -\left(C_{\text{correct}} \frac{\chi_m}{\mu_0} B_0 - S_z \frac{ge\hbar}{mm_e} \right) \eta > 0 \tag{27}$$

and z_0 is the amplitude. Here, we select the value of η corresponding to the second stage of the experiment to calculate the minimum accuracy required to control the magnetic field. This is because the fluctuation in the magnetic field is inversely proportional to A. The greater the value of A, the higher the accuracy requirements for the magnetic field control. Also, the value of A is proportional to η [Eq. (27)]. The larger

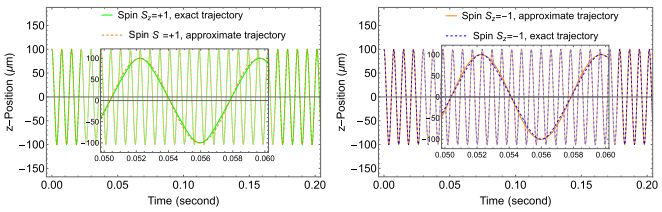

FIG. 9. Comparison of approximate and exact trajectories of two wave packets. Here, $m = 10^{-17}$ kg, $\eta = 1 \times 10^8$ T/m^2, $C_{\text{correct}} = 2526.82$, and $p_z = 0$.

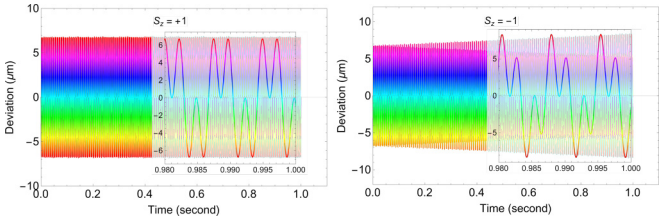

FIG. 10. The deviation between the approximate trajectory and the exact trajectory for $S_z = \pm 1$. Here, $m = 10^{-17}$ kg, $\eta = 1 \times 10^8$ T/m^2, $C_{\text{correct}} = 2526.82$, and $p_z = 0$.

the η, the larger A is. The value of η used in stage II of the experiment is the smallest, so the accuracy required to control the magnetic field will be the lowest at this stage; see expressions (37) and (38) below.

For $m = 10^{-17}$ kg (see Fig. 4), the value of $\eta = 1 \times 10^6$ T/m^2 at stage II, and the corresponding correction factor $C_{\text{correct}} = 27.3467$. The corrected approximate trajectory is compared with the exact trajectory as shown in Fig. 7 [72].

We can compare the approximated trajectory with the exact trajectory (see Fig. 7 for $m = 10^{-17}$ kg for 1.4 s and Fig. 8 for a longer time period, 5 s) for both the wave functions, i.e., up- and down-spin trajectories. Figure 8 shows the deviation of the approximate trajectory from the exact trajectory. We can see that the maximum deviation between the trajectories within 4 s is less than 10 μm.

With the abovementioned approximations, we can now address the question of spin coherence and any fluctuations in the magnetic field, i.e., any deviation $\Delta\eta$ in the value of η due to an inaccuracy in the control of the magnetic field. Then the deviation of the trajectory can be expressed as

$$\Delta z(t) = z_0 - z_0 \cos(\sqrt{A + \Delta A}t) \leqslant z_0 \frac{\Delta A^2}{4A} t^2, \tag{28}$$

where

$$\Delta A = -\left(C_{\text{correct}} \frac{\chi_m}{\mu_0} B_0 - S_z \frac{ge\hbar}{mm_e}\right) \Delta\eta. \tag{29}$$

Here, we have used $\sqrt{A}t = 2n\pi$ (n is a positive integer), and then we have $\cos(\sqrt{A}t) = 1$, $\sin(\sqrt{A}t) = 0$. Combining

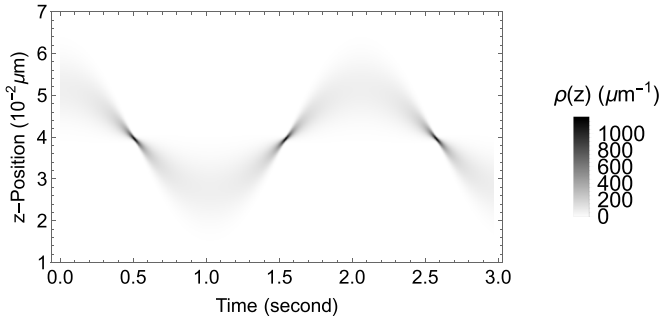

FIG. 11. The evolution of the wave packet for $S_z = -1$. The shadow in the figure corresponds to the probability density that the NV center is located at a certain spatial location at a certain time. The darker the color of the shadow, the greater the value of the probability density. Here, initial width of wave packet $\delta_z \approx 5 \times 10^{-3}$ μm, $m = 10^{-17}$ kg, and $\eta = 1 \times 10^6$ T/m^2.

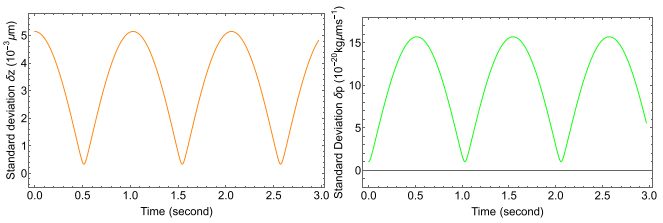

FIG. 12. The standard deviation for the z position and momentum for $S_z = -1$, where $\delta z = (\langle z^2\rangle - \langle z\rangle^2)^{\frac{1}{2}}$, $\delta p = (\langle p^2\rangle - \langle p\rangle^2)^{\frac{1}{2}}$. The standard deviation of the wave packet position and momentum shows a periodic oscillation behavior in the quartic potentials. Here, $m = 10^{-17}$ kg, and $\eta = 1 \times 10^6$ T/m^2.

Eqs. (23) and (27)–(29), we can get

$$\left(\frac{\Delta\eta}{\eta}\right)_z \leqslant \left(\frac{2\sqrt{2}\varepsilon}{z_0 A t^2}\delta z\right)^{\frac{1}{2}}, \tag{30}$$

where the subscript z represents the accuracy required to obtain from the positional uncertainty.

Similarly, by using the last inequality about the momentum in Eq. (23), we can also obtain a requirement for the accuracy of the magnetic field. The momentum can be obtained by taking the derivative of Eq. (26):

$$p_z(t) = m\frac{dz}{dt} = -mz_0\sqrt{A}\sin(\sqrt{A}t). \tag{31}$$

Since the initial momentum is zero, we can directly express the deviation of momentum as

$$\begin{aligned}\Delta p_z(t) &= -mz_0\sqrt{A+\Delta A}\sin(\sqrt{A+\Delta A}t) \\ &\leqslant mz_0\left(\sqrt{A}+\frac{\Delta A}{2\sqrt{A}}\right)\sin\left(\left(\sqrt{A}+\frac{\Delta A}{2\sqrt{A}}\right)t\right) \\ &= \frac{1}{4}\frac{mz_0 t}{A}(\Delta A + A)^2 - \frac{1}{4}mz_0 At.\end{aligned} \tag{32}$$

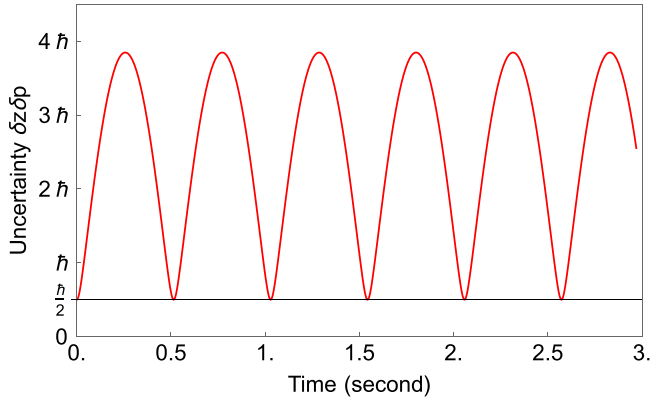

FIG. 13. The uncertainty of the position and the momentum of the wave packet for $S_z = -1$. The uncertainty changes periodically with time and satisfies the uncertainty principle $\delta_z\delta_p \geqslant \hbar/2$. Here, $m = 10^{-17}$ kg, and $\eta = 1 \times 10^6$ T/m^2.

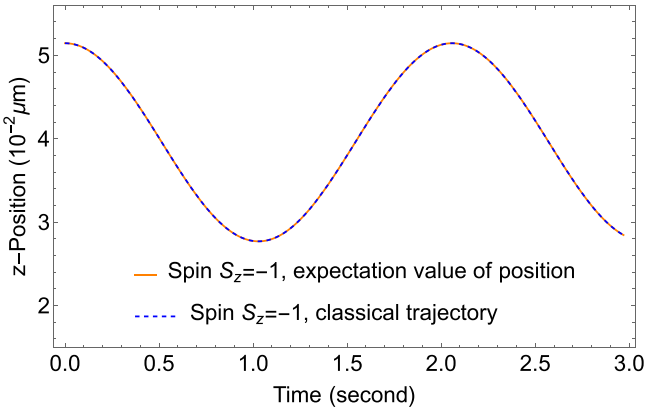

FIG. 14. Comparison between the expectation value of the NV center's position and the classical trajectory of the NV center. The two trajectories coincide. Here, $m = 10^{-17}$ kg, and $\eta = 1 \times 10^6$ T/m^2.

Here, we have also used $\cos(\sqrt{A}t) = 1$ and $\sin(\sqrt{A}t) = 0$. Combining Eqs. (23), (27), (29), and (32), we can get

$$\left(\frac{\Delta\eta}{\eta}\right)_{p_z} \leqslant \left(\frac{2\sqrt{2}\varepsilon}{mz_0At}\delta p_z + 1\right)^{\frac{1}{2}} - 1, \tag{33}$$

where the subscript p_z represents the accuracy required from the momentum uncertainty.

Using the approximate solution of the wave packet trajectory [Eq. (26)], when time t satisfies $\sqrt{A}t = 2n\pi$, the variation of the trajectory can be written as

$$(\delta z(t))^2 = (\delta z_0)^2 + \left(\frac{t}{m}\right)^2 (\delta p_z)^2. \tag{34}$$

If we require that the wave packet does not spread significantly in time t, then the last term in Eq. (34) needs to be satisfied [73]:

$$\frac{t}{m}\delta p_z \cong \delta z_0. \tag{35}$$

Combining Eq. (35) with the minimum uncertainty $\delta z = \delta p_z = (\hbar/2)^{\frac{1}{2}}$, we can get

$$\delta z = \left(\frac{t\hbar}{2m}\right)^{\frac{1}{2}}, \quad \delta p_z = \left(\frac{m\hbar}{2t}\right)^{\frac{1}{2}}. \tag{36}$$

By substituting Eq. (36) into Eqs. (30) and (33), we can get

$$\left(\frac{\Delta\eta}{\eta}\right)_z \leqslant \left(\frac{2\varepsilon\hbar^{\frac{1}{2}}}{z_0Am^{\frac{1}{2}}t^{\frac{3}{2}}}\right)^{\frac{1}{2}}, \tag{37}$$

$$\left(\frac{\Delta\eta}{\eta}\right)_{p_z} \leqslant \left(\frac{2\varepsilon\hbar^{\frac{1}{2}}}{z_0Am^{\frac{1}{2}}t^{\frac{3}{2}}} + 1\right)^{\frac{1}{2}} - 1. \tag{38}$$

Using Eqs. (37) and (38), we obtain the magnetic field accuracy required for masses to recover the spin coherence, as shown in Table I.

In Table I we have used $\varepsilon = 0.1$, which corresponds to recovering 99% spin coherence; $z_0 = 1 \times 10^{-4}$ m, which is the initial center position of the wave packet; $t = \frac{2\pi}{\sqrt{A}} \approx 0.7$ s, which is the duration of experimental stage; and $\eta = 1 \times 10^6$ T/m^2, which is the gradient parameter.

VI. CONCLUSION

In this paper, we have provided a simple mechanism for creating a large spatial superposition with heavy masses and with embedded spin. We have shown that it is possible to achieve $\Delta Z \sim O(10^3)$ μm for $m = 10^{-17}$ kg, $\Delta Z \sim O(10^2)$ μm for $m = 10^{-16}$ kg, and $\Delta Z \sim O(10)$ μm for $m = 10^{-15}$ kg within ∼1.4 s. There is indeed an order-of-magnitude gain in the splitting of the wave function compared with our earlier proposal [53], where we had taken only the gradient term in the magnetic field and could not achieve such a large spatial superposition in a short time scale (within 1–1.5 s). In this regard, catapulting the trajectory of the two wave packets has yielded a better result with a magnetic field gradient of order $O(10^2$–$10^4)$ T/m.

We highlighted that there are primarily three stages of the trajectory. First, we create a large velocity difference between the two wave packets, which experience differential spin-dependent forces. The anharmonic oscillations gradually increase the amplitude, and when the two trajectories meet at $z = 0$, their velocity difference is large, and the trajectories catapult to achieve a large spatial splitting. We employ three different values of the η parameter which controls the magnetic field gradient; see Fig. 4 and Appendix C, Figs. 15 and 16. We have ensured that the interference is completed within O(1–1.5) s, where the wave function overlap is such that the position and the momentum match to interfere with the two paths. We have also analyzed the conditions required to maintain the spin coherence. To achieve 99% coherence, we have obtained the stringent bound on the magnetic field fluctuations. The most stringent condition on the fluctuation in the magnetic field arises from stage I (see Appendix A, Table II), and similarly for stage II (see Table I). We have also analyzed the spreading of the wave function and showed that the wave packets evolve and do not satisfy the minimum uncertainty principle throughout the trajectory at every moment but that the largest $\delta z \delta p \leqslant 4\hbar$ (this restriction only holds when the initial conditions are $\delta z \sim 5 \times 10^{-3}$ μm and the initial position $z \sim 5 \times 10^{-2}$ μm) and it oscillates with a period of roughly 0.5 s where it satisfies the minimum uncertainty principle for $m = 10^{-17}$ kg and for $\eta = 10^6$ T/m^2. However, the wave function's classical and quantum trajectories match extremely well; see Appendix B, Fig. 14.

Indeed, in all of our analysis, the time duration of the spin coherence is an important factor for the experiment, but the spin coherence times are perpetually rising (approaching 1 s [69,70], even 30 s [74,75]); adapting these to nanocrystals remains an open problem, but there are no fundamental constraints [76]. The spatial coherence times can be made 100 s; see Refs. [7,21,23]. There are indeed other challenges, but the requisite pressures, temperatures, distances from other sources, and fluctuations are achievable [23]. For example, a decoherence rate below 0.1 Hz is achievable for diamond

spheres of masses 10^{-14} kg. This is expected [7,23] for internal temperatures of 0.15 K, an environmental temperature of 1 K, and the environmental gas number density of 10^{-8} m^{-3}. In addition to these, we will need to take into account the effect of the rotation of the diamond [65] and the excitation of phonons [77] on the spin coherence. However, we will study these effects separately.

ACKNOWLEDGMENTS

We would like to thank Y. Japha, R. Folman, and B. Stickler for discussions. R.Z. is supported by a China Scholarship Council (CSC) fellowship. R.J.M. is supported by the Australian Research Council (ARC) under the Centre of Excellence for Quantum Computation and

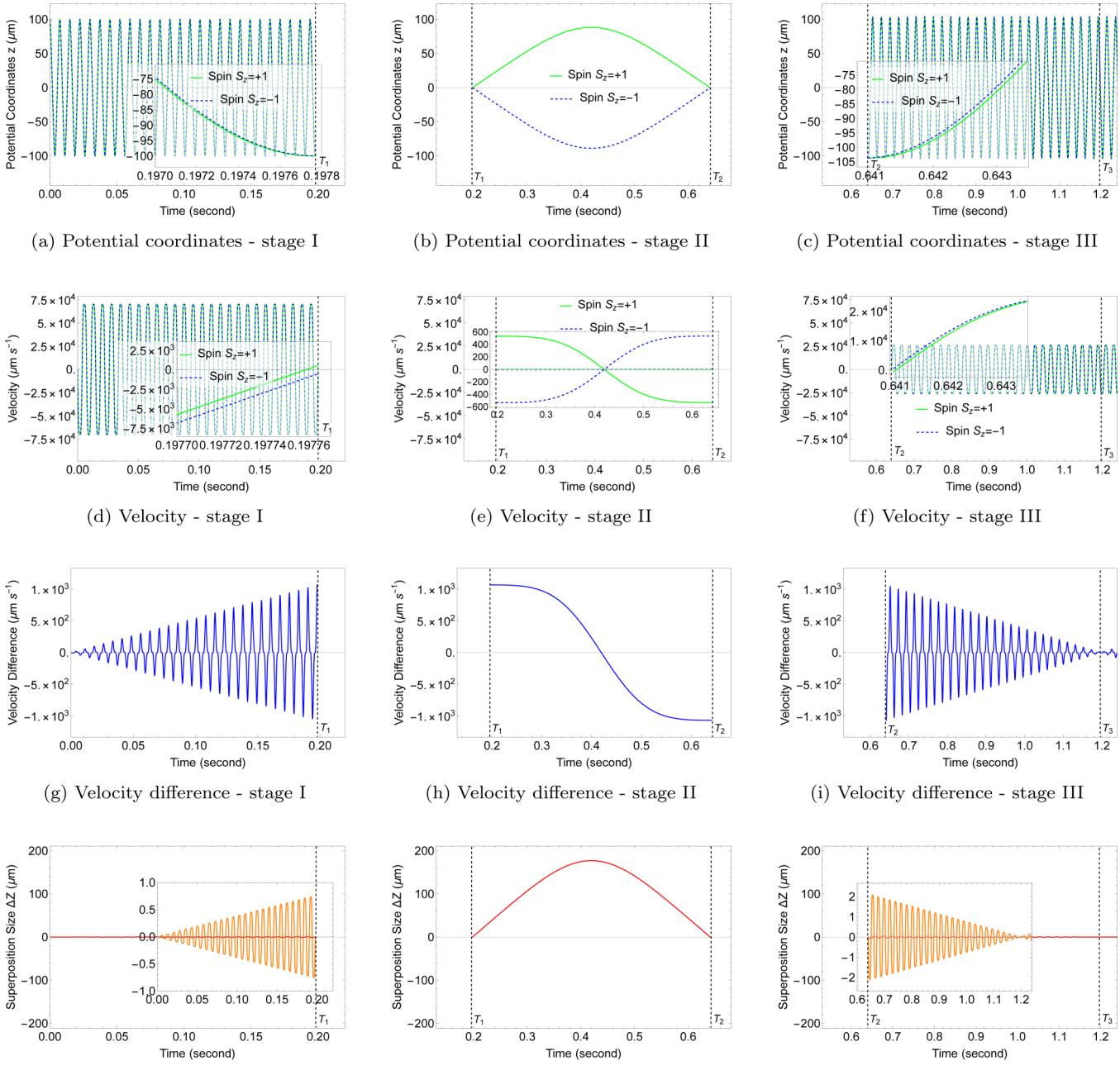

(a) Potential coordinates - stage I (b) Potential coordinates - stage II (c) Potential coordinates - stage III

(d) Velocity - stage I (e) Velocity - stage II (f) Velocity - stage III

(g) Velocity difference - stage I (h) Velocity difference - stage II (i) Velocity difference - stage III

(j) Superposition size - stage I (k) Superposition size - stage II (l) Superposition size - stage III

FIG. 15. Dynamical aspects for the mass $m = 10^{-16}$ kg during the three experimental stages: (a)–(c) the magnetic field coordinates (potential coordinates) experienced, (d)–(f) the velocities, (g)–(i) the velocity differences, and (j)–(l) the superposition size. We set different values of η and the initial position of the wave packet in the magnetic field at different stages. Stage I , $\eta = 1 \times 10^8$ T/m^2, with initial coordinate $z = 100$ μm. Stage II , $\eta = 9 \times 10^5$ T/m^2, with initial coordinate $z = 0$ μm. Stage III , $\eta = 3.445 \times 10^7$ T/m^2, with initial coordinate $z = -103.7$ μm. Times T_1 and T_2 are determined by constraining the moment when the superposition size is zero (with an accuracy of $z = 10^{-6}$ μm). Time T_3 is the moment when both the velocity difference between the two wave packets and the superposition size are zero.

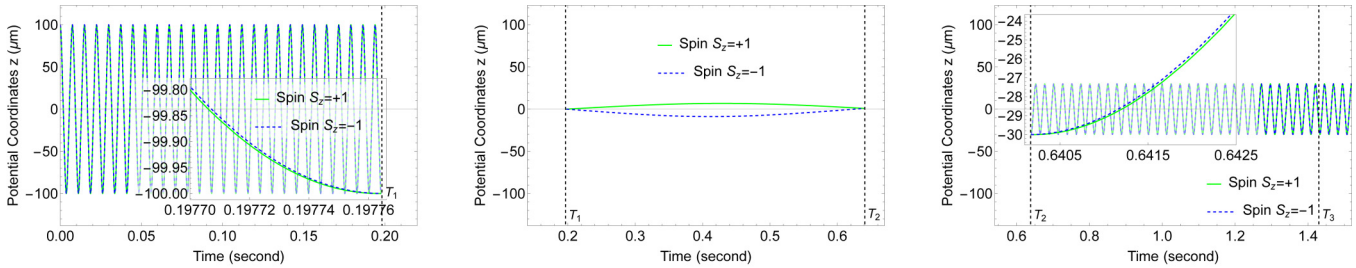

(a) Potential coordinates - stage I (b) Potential coordinates - stage II (c) Potential coordinates - stage III

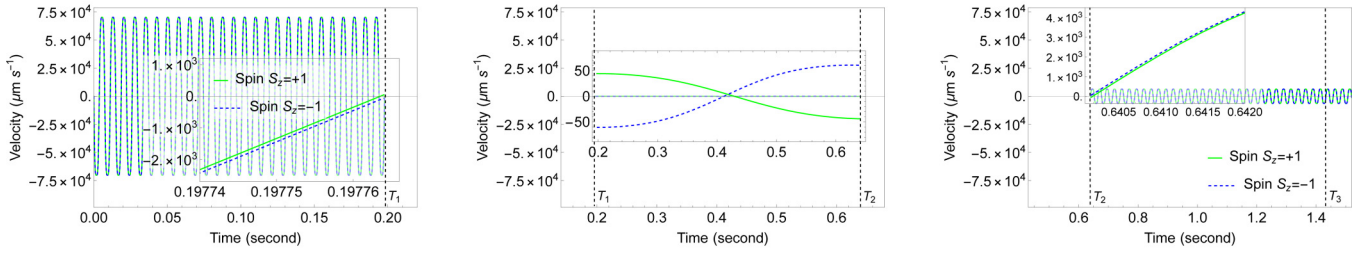

(d) Velocity - stage I (e) Velocity - stage II (f) Velocity - stage III

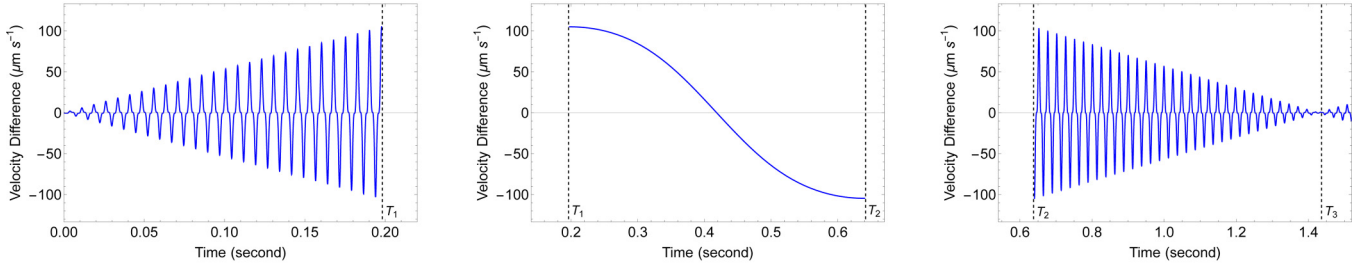

(g) Velocity difference - stage I (h) Velocity difference - stage II (i) Velocity difference - stage III

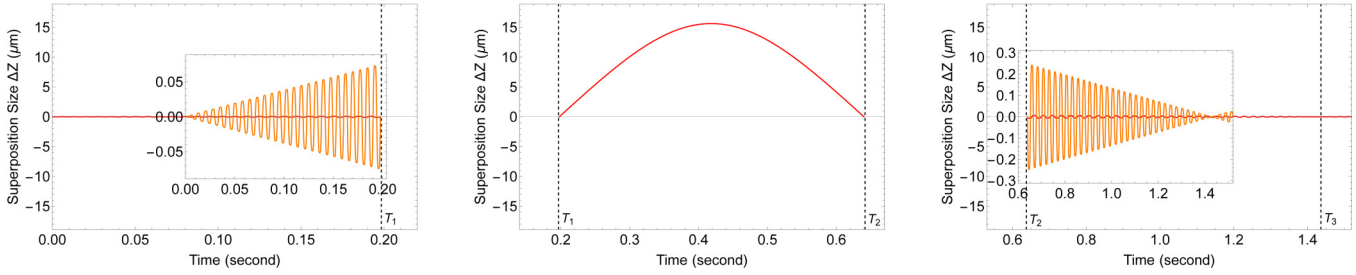

(j) Superposition size - stage I (k) Superposition size - stage II (l) Superposition size - stage III

FIG. 16. Dynamics for the mass $m = 10^{-15}$ kg during the three experimental stages: (a)–(c) the magnetic field coordinates (potential coordinates) experienced, (d)–(f) the velocities, (g)–(i) the velocity differences, and (j)–(l) the superposition size. We set different values of η and the initial position of the wave packet in the magnetic field at different stages. Stage I , $\eta = 1 \times 10^8$ T/m^2, corresponding to the coordinate $z = 100$ μm. Stage II , $\eta = 6 \times 10^6$ T/m^2, corresponding to the initial coordinate $z = 0$ μm. Stage III , $\eta = 1 \times 10^8$ T/m^2, with an initial coordinate $z = -30$ μm. Times T_1 and T_2 are determined by constraining the moment when the superposition size is zero (with an accuracy of $z = 10^{-6}$ μm). Time T_3 is the moment when both the velocity difference between the two wave packets and the superposition size are zero.

Communication Technology (Project No. CE170100012). A.M.'s research is funded by Netherlands Organisation for Science and Research (NWO) Grant No. 680-91-119. S.B. would like to acknowledge EPSRC Grants No. EP/N031105/1 and No. EP/S000267/1.

APPENDIX A: SPIN COHERENCE AND MAGNETIC FIELD CONTROL FOR $\eta = 1 \times 10^8$ T/m^2

According to the analysis in Sec. V, we can calculate the accuracy required for the magnetic field control under the new magnetic field gradient by directly replacing the

corresponding values of η and the correction factor. Now we set $\eta = 1 \times 10^8$ T/m^2 and the corresponding correction factor $C_{\text{correct}} = 2526.82$. Using Eqs. (5) and (26), we can compare the approximate and the exact trajectories of the wave packets as shown in Fig. 9.

Figure 10 shows the deviation of the approximate trajectory from the exact trajectory. We can see that the maximum deviation between trajectories within 1 s is less than 9 μm.

Using Eqs. (37) and (38), we can get $\delta\eta/\eta$ in the magnetic field fluctuation for different masses, as shown in Table II.

In Table II we have used $\varepsilon = 0.1$, which corresponds to maintaining 99% spin coherence; $z_0 = 1 \times 10^{-4}$ m, which is the initial center position of the wave packet; $t = \frac{60\pi}{\sqrt{A}} \approx 0.2$ s, which is the duration of the experimental stage; and $\eta = 1 \times 10^8$ T/m^2, which is the gradient parameter.

APPENDIX B: SPREADING OF THE WAVE PACKET

In Sec. V, we assumed that the wave packet is always kept to a minimum uncertainty when calculating the accuracy required of the magnetic field control to restore spin coherence. In this Appendix, we study the evolution of the wave packet width in the quartic potentials, providing a theoretical basis for our hypothesis in Sec. V.

The Schrödinger equation is

$$i\hbar\frac{d}{dt}|\Psi(t)\rangle = \hat{H}|\Psi(t)\rangle. \tag{B1}$$

By substituting the specific forms of the Hamiltonian [Eq. (1)] and magnetic field [Eq. (4)] into the Schrödinger equation and making the initial state the Gaussian wave packet shown in Eq. (20), we can use the Trotter expansion method to numerically calculate the evolution of the wave packet [78] as shown in Fig. 11.

It can be seen from Fig. 11 that the spreading of the wave packet in the quartic potential exhibits a periodic oscillation behavior. For the purpose of illustration, we will take a single value of $\eta = 10^6$ T/m^2 for mass $m = 10^{-17}$ kg. A similar analysis can be performed for different values of η, but the physical properties will not alter much.

The uncertainty of the position and momentum of the wave packet is shown in Fig. 12. The product of the uncertainty of position and momentum satisfies the uncertainty principle, as shown in Fig. 13. As can be seen from Fig. 13, the value of $\delta_z\delta_p$ changes periodically over time and returns to the minimum uncertainty at the end of a period, which means that our assumptions in Sec. V are reasonable.

In order to verify the correctness of the numerical results, we compare the expectation value of the wave packet position with the classical trajectory as shown in Fig. 14.

As can be seen from Fig. 14, the expectation value of the wave packet position coincides with the classical trajectory [Eq. (5)], which means that our numerical calculation of the evolution of the wave packet is correct.

APPENDIX C: TRAJECTORIES FOR MASSES 10^{-16} AND 10^{-15} kg

The time evolution of the nanocrystals for different masses in a nonlinear magnetic field shows a very similar pattern to that of $m = 10^{-17}$ kg. The main difference between these evolutions is that the maximum velocity difference between the wave packets with the opposite spin orientations is inversely proportional to the mass for the same magnetic field gradient parameter η (Fig. 6). The difference in velocity between the wave packets then determines the superposition size that we can obtain in the same time span. The magnetic field used to control the motion of the wave packets in the second and third stages will change accordingly for different masses and the difference in velocity between the wave packets at the end of the first stage. We have shown the numerical results of specific parameters and the evolution of the nanocrystals in Figs. 15 and 16. An important point to note is that for the heaviest mass $m = 10^{-15}$ kg we can obtain the spatial superposition size of 15 μm, which is the required valued we require for testing the quantum nature of gravity in a laboratory by including the Casimir screening; see Ref. [23]. The simple scaling of the superposition size ΔZ_0 is given by Eq. (10).

[1] C. Kiefer, *Quantum Gravity* (Oxford University Press, Oxford, 2014).

[2] C. M. Will, The confrontation between general relativity and experiment, Living Rev. Relativ. **17**, 4 (2014).

[3] J. Martin and V. Vennin, Obstructions to Bell CMB experiments, Phys. Rev. D **96**, 063501 (2017).

[4] A. Ashoorioon, P. S. Bhupal Dev, and A. Mazumdar, Implications of purely classical gravity for inflationary tensor modes, Mod. Phys. Lett. A **29**, 1450163 (2014).

[5] A. Addazi, J. Alvarez-Muniz, R. Alves Batista, G. Amelino-Camelia, V. Antonelli, M. Arzano, M. Asorey, J.-L. Atteia, S. Bahamonde, F. Bajardi, A. Ballesteros, B. Baret, D. M. Barreiros, S. Basilakos, D. Benisty, O. Birnholtz, J. J. Blanco-Pillado, D. Blas, J. Bolmont, D. Boncioli *et al.*, Quantum gravity phenomenology at the dawn of the multi-messenger era—A review, Prog. Part. Nucl. Phys. **125**, 103948 (2022).

[6] F. Dyson, Is a graviton detectable? in *XVIIth International Congress on Mathematical Physics* (World Scientific, Singapore, 2014), pp. 670–682.

[7] S. Bose, A. Mazumdar, G. W. Morley, H. Ulbricht, M. Toroš, M. Paternostro, A. Geraci, P. Barker, M. S. Kim, and G. Milburn, Spin Entanglement Witness for Quantum Gravity, Phys. Rev. Lett. **119**, 240401 (2017).

[8] C. Marletto and V. Vedral, Gravitationally Induced Entanglement between Two Massive Particles is Sufficient Evidence of Quantum Effects in Gravity, Phys. Rev. Lett. **119**, 240402 (2017).

[9] R. J. Marshman, A. Mazumdar, and S. Bose, Locality and entanglement in table-top testing of the quantum nature of linearized gravity, Phys. Rev. A **101**, 052110 (2020).

[10] S. Bose, A. Mazumdar, M. Schut, and M. Toroš, Mechanism for the quantum natured gravitons to entangle masses, Phys. Rev. D **105**, 106028 (2022).

[11] M. Christodoulou, A. Di Biagio, M. Aspelmeyer, Č. Brukner, C. Rovelli, and R. Howl, Locally mediated entanglement through gravity from first principles, arXiv:2202.03368 [quant-ph].

[12] D. L. Danielson, G. Satishchandran, and R. M. Wald, Gravitationally mediated entanglement: Newtonian field versus gravitons, Phys. Rev. D **105**, 086001 (2022).

[13] A. J. Leggett, Testing the limits of quantum mechanics: motivation, state of play, prospects, J. Phys.: Condens. Matter **14**, R415 (2002).

[14] M. Arndt and K. Hornberger, Testing the limits of quantum mechanical superpositions, Nat. Phys. **10**, 271 (2014).

[15] P. F. Barker, S. Bose, R. J. Marshman, and A. Mazumdar, Entanglement based tomography to probe new macroscopic forces, Phys. Rev. D **106**, L041901 (2022).

[16] S. Bose, A. Mazumdar, M. Schut, and M. Toroš, Entanglement witness for the weak equivalence principle, arXiv:2203.11628 [gr-qc].

[17] R. Penrose, On gravity's role in quantum state reduction, Gen. Rel. Gravitation **28**, 581 (1996); Quantum computation, entanglement and state reduction, Philos. Trans. R. Soc., A **356**, 1927 (1998); L. Diosi, Gravitation and the quantum-mechanical localization of macro-objects, Phys. Lett. A **105**, 199 (1984); A universal master equation for the gravitational violation of quantum mechanics, **120**, 377 (1987).

[18] A. Bassi, K. Lochan, S. Satin, T. P. Singh, and H. Ulbricht, Models of wave-function collapse, underlying theories, and experimental tests, Rev. Mod. Phys. **85**, 471 (2013).

[19] E. Joos and H. D. Zeh, The emergence of classical properties through interaction with the environment, Z. Phys. B: Condens. Matter **59**, 223 (1985).

[20] M. A. Schlosshauer, *Decoherence and the Quantum-to-Classical Transition* (Springer, New York, 2007); Quantum decoherence, Phys. Rep. **831**, 1 (2019).

[21] M. Toroš, T. W. Van De Kamp, R. J. Marshman, M. S. Kim, A. Mazumdar, and S. Bose, Relative acceleration noise mitigation for nanocrystal matter-wave interferometry: Applications to entangling masses via quantum gravity, Phys. Rev. Res. **3**, 023178 (2021).

[22] R. J. Marshman, A. Mazumdar, G. W. Morley, P. F. Barker, S. Hoekstra, and S. Bose, Mesoscopic interference for metric and curvature (MIMAC) & gravitational wave Ddetection, New J. Phys. **22**, 083012 (2020).

[23] T. W. van de Kamp, R. J. Marshman, S. Bose, and A. Mazumdar, Quantum gravity witness via entanglement of masses: Casimir screening, Phys. Rev. A **102**, 062807 (2020).

[24] M. Arndt, O. Nairz, J. Vos-Andreae, C. Keller, G. van der Zouw, and A. Zeilinger, Wave–particle duality of C_{60} molecules, Nature (London) **401**, 680 (1999).

[25] S. Nimmrichter and K. Hornberger, Macroscopicity of Mechanical Quantum Superposition States, Phys. Rev. Lett. **110**, 160403 (2013).

[26] T. Kovachy, P. Asenbaum, C. Overstreet, C. A. Donnelly, S. M. Dickerson, A. Sugarbaker, J. M. Hogan, and M. A. Kasevich, Quantum superposition at the half-metre scale, Nature (London) **528**, 530 (2015).

[27] Y. Y. Fein, P. Geyer, P. Zwick, F. Kiałka, S. Pedalino, M. Mayor, S. Gerlich, and M. Arndt, Quantum superposition of molecules beyond 25 kDa, Nat. Phys. **15**, 1242 (2019).

[28] S. Bose, K. Jacobs, and P. L. Knight, Scheme to probe the decoherence of a macroscopic object, Phys. Rev. A **59**, 3204 (1999).

[29] A. D. Armour, M. P. Blencowe, and K. C. Schwab, Entanglement and Decoherence of a Micromechanical Resonator via Coupling to a Cooper-Pair Box, Phys. Rev. Lett. **88**, 148301 (2002).

[30] W. Marshall, C. Simon, R. Penrose, and D. Bouwmeester, Towards Quantum Superpositions of a Mirror, Phys. Rev. Lett. **91**, 130401 (2003).

[31] P. Sekatski, M. Aspelmeyer, and N. Sangouard, Macroscopic Optomechanics from Displaced Single-Photon Entanglement, Phys. Rev. Lett. **112**, 080502 (2014).

[32] O. Romero-Isart, M. L. Juan, R. Quidant, and J. I. Cirac, Toward quantum superposition of living organisms, New J. Phys. **12**, 033015 (2010).

[33] O. Romero-Isart, A. C. Pflanzer, F. Blaser, R. Kaltenbaek, N. Kiesel, M. Aspelmeyer, and J. I. Cirac, Large Quantum Superpositions and Interference of Massive Nanometer-Sized Objects, Phys. Rev. Lett. **107**, 020405 (2011).

[34] F. Khalili, S. Danilishin, H. Miao, H. Müller-Ebhardt, H. Yang, and Y. Chen, Preparing a Mechanical Oscillator in Non-Gaussian Quantum States, Phys. Rev. Lett. **105**, 070403 (2010).

[35] M. Scala, M. S. Kim, G. W. Morley, P. F. Barker, and S. Bose, Matter-Wave Interferometry of a Levitated Thermal Nano-Oscillator Induced and Probed by a Spin, Phys. Rev. Lett. **111**, 180403 (2013).

[36] C. Wan, M. Scala, G. W. Morley, A. A. Rahman, H. Ulbricht, J. Bateman, P. F. Barker, S. Bose, and M. S. Kim, Free Nano-Object Ramsey Interferometry for Large Quantum Superpositions, Phys. Rev. Lett. **117**, 143003 (2016).

[37] J. Bateman, S. Nimmrichter, K. Hornberger, and H. Ulbricht, Near-field interferometry of a free-falling nanoparticle from a point-like source, Nat. Commun. **5**, 4788 (2014).

[38] Z. Q. Yin, T. Li, X. Zhang, and L. M. Duan, Large quantum superpositions of a levitated nanodiamond through spin-optomechanical coupling, Phys. Rev. A **88**, 033614 (2013).

[39] H. Pino, J. Prat-Camps, K. Sinha, B. P. Venkatesh, and O. Romero-Isart, On-chip quantum interference of a superconducting microsphere, Quantum Sci. Technol. **3**, 025001 (2018).

[40] J. Clarke and M. R. Vanner, Growing macroscopic superposition states via cavity quantum optomechanics, Quantum Sci. Technol. **4**, 014003 (2019).

[41] M. Ringbauer, T. J. Weinhold, L. A. Howard, A. G. White, and M. R. Vanner, Generation of mechanical interference fringes by multi-photon counting, New J. Phys. **20**, 053042 (2018).

[42] K. E. Khosla, M. R. Vanner, N. Ares, and E. A. Laird, Displacemon Electromechanics: How to Detect Quantum Interference in a Nanomechanical Resonator, Phys. Rev. X **8**, 021052 (2018).

[43] R. Kaltenbaek, G. Hechenblaikner, N. Kiesel, O. Romero-Isart, K. C. Schwab, U. Johann, and M. Aspelmeyer, Macroscopic quantum resonators (MAQRO), Exp. Astron. **34**, 123 (2012).

[44] O. Romero-Isart, Coherent inflation for large quantum superpositions of levitated microspheres, New J. Phys. **19**, 123029 (2017).

[45] J. S. Pedernales, G. W. Morley, and M. B. Plenio, Motional Dynamical Decoupling for Interferometry with Macroscopic Particles, Phys. Rev. Lett. **125**, 023602 (2020).

[46] J. M. Hogan, D. Johnson, and M. A. Kasevich, Light-pulse atom interferometry, arXiv:0806.3261 [physics.atom-ph].

[47] S. Machluf, Y. Japha, and R. Folman, Coherent Stern-Gerlach momentum splitting on an atom chip, Nat. Commun. **4**, 2424 (2013).

[48] Y. Margalit, O. Dobkowski, Z. Zhou, O. Amit, Y. Japha, S. Moukouri, D. Rohrlich, A. Mazumdar, S. Bose, C. Henkel, and R. Folman, Realization of a complete Stern-Gerlach interferometer: Toward a test of quantum gravity, Sci. Adv. **7**, eabg2879 (2021).

[49] A. Al Balushi, W. Cong, and R. B. Mann, Optomechanical quantum Cavendish experiment, Phys. Rev. A **98**, 043811 (2018).

[50] B. D. Wood, S. Bose, and G. W. Morley, Spin dynamical decoupling for generating macroscopic superpositions of a free-falling nanodiamond, Phys. Rev. A **105**, 012824 (2022).

[51] C. Gonzalez-Ballestero, M. Aspelmeyer, L. Novotny, R. Quidant, and O. Romero-Isart, Levitodynamics: Levitation and control of microscopic objects in vacuum, Science **374**, eabg3027 (2021).

[52] J. F. Hsu, P. Ji, C. W. Lewandowski, and B. D'Urso, Cooling the motion of diamond nanocrystals in a magneto-gravitational trap in high vacuum, Sci. Rep. **6**, 30125 (2016).

[53] R. J. Marshman, A. Mazumdar, R. Folman, and S. Bose, Constructing nano-object quantum superpositions with a Stern-Gerlach interferometer, Phys. Rev. Res. **4**, 023087 (2022).

[54] M. M. Paraniak and B.-G. Englert, Quantum dynamical simulation of a transversal Stern-Gerlach interferometer, Symmetry **13**, 1660 (2021).

[55] E. Majorana, Atomi orientati in campo magnetico variabile, Nuovo Cimento **9**, 43 (1932).

[56] M. Inguscio, Majorana "spin-flip" and ultra-low temperature atomic physics, in *International Conference on Ettore Majorana's Legacy and the Physics of the XXI Century*, Proceedings of Science Vol. 37 (Università degli Studi di Catania, Catania, Italy, 2007), p. 008.

[57] J. Tilly, R. J. Marshman, A. Mazumdar, and S. Bose, Qudits for witnessing quantum-gravity-induced entanglement of masses under decoherence, Phys. Rev. A **104**, 052416 (2021); M. Schut, J. Tilly, R. J. Marshman, S. Bose, and A. Mazumdar, Improving resilience of quantum-gravity-induced entanglement of masses to decoherence using three superpositions, *ibid.* **105**, 032411 (2022).

[58] B.-G. Englert, J. Schwinger, and M. O. Scully, Is spin coherence like Humpty-Dumpty? I. Simplified treatment, Found. Phys. **18**, 1045 (1988).

[59] J. Schwinger, M. O. Scully, and B.-G. Englert, Is spin coherence like Humpty-Dumpty? II. General theory, Z. Phys. D: At., Mol. Clusters **10**, 135 (1988).

[60] J. H. N. Loubser and J. A. van Wyk, Electron spin resonance in the study of diamond, Rep. Prog. Phys. **41**, 1201 (1978).

[61] S. Kuhn, A. Kosloff, B. A. Stickler, F. Patolsky, K. Hornberger, M. Arndt, and J. Millen, Full rotational control of levitated silicon nanorods, Optica **4**, 356 (2017).

[62] J. Schäfer, H. Rudolph, K. Hornberger, and B. A. Stickler, Cooling Nanorotors by Elliptic Coherent Scattering, Phys. Rev. Lett. **126**, 163603 (2021).

[63] H. Rudolph, J. Schafer, B. A. Stickler, and K. Hornberger, Theory of nanoparticle cooling by elliptic coherent scattering, Phys. Rev. A **103**, 043514 (2021).

[64] F. van der Laan, F. Tebbenjohanns, R. Reimann, J. Vijayan, L. Novotny, and M. Frimmer, Sub-Kelvin Feedback Cooling and Heating Dynamics of an Optically Levitated Librator, Phys. Rev. Lett. **127**, 123605 (2021).

[65] Y. Japha and R. Folman, Role of rotations in Stern-Gerlach interferometry with massive objects, arXiv:2202.10535 [quant-ph].

[66] We can test that the magnetic field function satisfies Maxwell's equation $\nabla \cdot \mathbf{B} = \mathbf{0}$ and $\nabla \times \mathbf{B} = \mathbf{0}$ away from the source term.

[67] The actual magnetic field gradient is small, as $\partial B/\partial z \sim \eta z$ and $z \ll 1$ m. For $z \sim 100$ μm, the maximum magnetic field gradient will then be $\partial B/\partial z \sim \eta z \sim 10^4$ T/m. These values of the magnetic field gradient can be achievable in a laboratory [47,68].

[68] M. Modena, J. Garcia Perez, P. Thonet, C. Petrone, A. Vorozhtsov, O. Dunkel, E. Solodko, and D. Tomasini, Design, assembly and first measurements of a short model for CLIC final focus hybrid quadrupole QD0, in *Proceedings, 3rd International Particle Accelerator Conference (IPAC 2012)*, *Conference Proceedings C*, Vol. 1205201 (IEEE, Piscataway, NJ, 2012), pp. 3515–3517.

[69] N. Bar-Gill, L. M. Pham, A. Jarmola, D. Budker, and R. L. Walsworth, Solid-state electronic spin coherence time approaching one second, Nat. Commun. **4**, 1743 (2013).

[70] M. H. Abobeih, J. Cramer, M. A. Bakker, N. Kalb, M. Markham, D. J. Twitchen, and T. H. Taminiau, One-second coherence for a single electron spin coupled to a multi-qubit nuclear-spin environment, Nat. Commun. **9**, 2552 (2018).

[71] H. J. Mamin, C. T. Rettner, M. H. Sherwood, L. Gao, and D. Rugar, High field-gradient dysprosium tips for magnetic resonance force microscopy, Appl. Phys. Lett. **100**, 013102 (2012).

[72] We have performed a similar analysis for stage I of the trajectory, where $\eta = 10^8$ T/m^2 for different masses; see Appendix A for a discussion, and see Table II. The constraints on η for stage III will be very similar to those of stage I.

[73] See Appendix B, where we analyze the spread in the wave packet: Figure 11 shows the evolution of the probability density of the wave packet for one of the spins for $m = 10^{-17}$ kg for $\eta = 10^6$ T/m^2. The numerical values will not alter much for different values of η. Note that the expectation value of the wave packet position with the classical trajectory is shown in Fig. 14. We can see from Fig. 13 that the minimum uncertainty is not always followed throughout the trajectory but it is satisfied at certain times. If we could manage to close the interference at those moments, we would be able to recover the spin coherence as desired in the text.

[74] J. T. Muhonen, J. P. Dehollain, A. Laucht, F. E. Hudson, R. Kalra, T. Sekiguchi, K. M. Itoh, D. N. Jamieson, J. C. McCallum, A. S. Dzurak, and A. Morello, Storing quantum information for 30 seconds in a nanoelectronic device, Nat. Nanotechnol. **9**, 986 (2014).

[75] D. Farfurnik, A. Jarmola, L. M. Pham, Z. H. Wang, V. V. Dobrovitski, R. L. Walsworth, D. Budker, and N. Bar-Gill, Optimizing a dynamical decoupling protocol for solid-state

electronic spin ensembles in diamond, Phys. Rev. B **92**, 060301(R) (2015).

[76] H. S. Knowles, D. M. Kara, and M. Atatüre, Observing bulk diamond spin coherence in high-purity nanodiamonds, Nat. Mater. **13**, 21 (2014).

[77] C. Henkel and R. Folman, Internal decoherence in nano-object interferometry due to phonons, AVS Quantum Sci. **4**, 025602 (2022).

[78] R. Schmied, *Using Mathematica for Quantum Mechanics* (Springer, Singapore, 2020).